

This is a pre print version of the following article:

Thermal effects of pyroxenites on mantle melting below mid-ocean ridges / Brunelli, Daniele; Cipriani, Anna; Bonatti, Enrico. - In: NATURE GEOSCIENCE. - ISSN 1752-0908. - 11:7(2018), pp. 520-525. [10.1038/s41561-018-0139-z]

*Terms of use:*

The terms and conditions for the reuse of this version of the manuscript are specified in the publishing policy. For all terms of use and more information see the publisher's website.

03/05/2026 15:19

(Article begins on next page)

1 **Melting below Mid Ocean Ridges: thermal effects of pyroxenites in the peridotitic**  
2 **mantle**

3

4 Daniele Brunelli<sup>1,2\*</sup>, Anna Cipriani<sup>1,3\*</sup>, Enrico Bonatti<sup>2,3</sup>

5 <sup>1</sup> Dipartimento di Scienze Chimiche e Geologiche, Università di Modena e Reggio  
6 Emilia, Via Campi 103, 41125 Modena, Italy.

7 <sup>2</sup> Istituto di Scienze Marine, CNR, Via Gobetti 101, 40129 Bologna, Italy.

8 <sup>3</sup> Lamont Doherty Earth Observatory, Columbia University, Palisades, New York 10964,  
9 USA.

10

11 \* Corresponding authors: [daniele.brunelli@unimore.it](mailto:daniele.brunelli@unimore.it); [anna.cipriani@unimore.it](mailto:anna.cipriani@unimore.it)

12

13 *After travelling in the Earth's interior for up to billions of years, recycled material once*  
14 *injected at subduction zones can reach a subridge melting region as pyroxenite dispersed*  
15 *in the host peridotitic mantle. We studied genetically related crustal basalts and mantle*  
16 *peridotites sampled along an uplifted lithospheric section created at a segment of the Mid*  
17 *Atlantic Ridge through a time interval of 26 Ma. The arrival of low-solidus material into*  
18 *the melting region forces the elemental and isotopic imprint of the residual peridotites and*  
19 *of the basalts to diverge with time. We show that a pyroxenite-bearing source entering the*  
20 *subridge melting region induces undercooling of the host peridotitic mantle, due to*  
21 *subtraction of latent heat by melting of the low-T solidus pyroxenite. Mantle undercooling*  
22 *in turn lowers the thermal boundary layer leading to a deeper cessation of melting. A*  
23 *consequence is to decrease the total amount of extracted melt, hence magmatic crustal*  
24 *thickness. The degree of melting undergone by a homogeneous peridotitic mantle is higher*  
25 *than the degree of melting of the same peridotite but veined by pyroxenites. This effect,*  
26 *thermodynamically predicted for a marble-cake type peridotite-pyroxenite mixed source,*  
27 *implies incomplete homogenisation of recycled material in the convective mantle.*

28

30 Mantle rising beneath the 60,000 km long Mid Oceanic Ridge system contains, as in a  
31 slow-motion movie, a record of ancient upwelling and melting events and of interaction  
32 with subduction or hot spot-derived components. It is difficult to reconstruct temporal  
33 records of these ancient events due to lack of suitable samples; however, we were given  
34 the opportunity to explore the temporal evolution of the oceanic lithosphere composition  
35 and structure at 11°N along the Mid Atlantic Ridge (MAR) where an uplifted > 300 km  
36 long sliver of lithosphere exposes a basal mantle peridotite unit, lower crustal gabbros, a  
37 dyke complex and erupted basalts<sup>1-3</sup>. This lithospheric section (Vema Lithospheric Section  
38 or VLS) was generated at an 80 km long segment of the MAR (EMAR segment,  
39 Supplementary Fig. S1) during a 26 Ma time interval<sup>1,2,4-6</sup>. Both crustal basalts and their  
40 mantle peridotite parents have been densely sampled at the VLS along a seafloor spreading  
41 flow line<sup>4</sup> allowing comparisons of their isotopic and elemental composition throughout  
42 the 26 Ma time interval<sup>1,2,4-6</sup> (Fig. 1).

43 Surprisingly, temporal variations of mantle degree of melting estimated from basalt  $\text{Na}_8$ <sup>7,8</sup>  
44 anti-correlate with the degree of melting derived from spinel Cr# of the peridotites<sup>9,10</sup>,  
45 although the two curves converge to a common value in the youngest 3 Ma stretch of the  
46 VLS (Fig. 1). Older, isotopically enriched basalts display the lower  $\text{Na}_8$  values of the entire  
47 VLS, suggesting they were generated by a higher degree of melting of their mantle source;  
48 in contrast, the genetically associated mantle peridotites record a relatively low extent of  
49 melting, in agreement with a thinner crust recorded by geophysical data<sup>1</sup>. This anti-  
50 correlation contrasts with what is inferred to be the “normal” signature of partial melting at  
51 mid-ocean ridges.

52 We offer a solution to this conundrum by suggesting that a subridge variably veined  
53 mantle hosts chemically enriched, fertile, low-T melting components, i.e. pyroxenites.  
54 Thermodynamic-based studies predict dramatic effects when pyroxenites are present in the  
55 mantle source and partially melt along a decompressive path<sup>11-15</sup>. Low-T solidus  
56 components lower the extent of melting of the host peridotite due to subtraction of latent  
57 heat of fusion<sup>13-15</sup>. Pyroxenites melt preferentially, generating isotopically enriched, low  
58  $\text{Na}_8$  melts and cooling the host mantle peridotites, thereby lowering the degree of melting  
59 of the peridotite mantle in proportion to its pyroxenite content<sup>13</sup>. In this work we account  
60 for variable extents of the melting column by assuming that different pyroxenitic contents

61 result in variable extent of undercooling before the ambient peridotite starts melting. This  
62 situation mimics varying the potential temperature of the mantle resulting in changes in the  
63 length of the melting column.

64

65

66 Temporal variability of crustal thickness and mantle degree of melting

67

68 Basalt Nd, Sr and Pb isotopes vary coherently along the 26 Ma-long VLS section,  
69 showing a decrease in isotopic enrichment towards younger ages that hints at temporal  
70 variations of composition and thermal state of the rising mantle<sup>8</sup>. We represent these  
71 variations as discrete steps (Fig. 1a), defining three time domains: 0-2 Ma, 2-13 Ma and  
72 13-26 Ma (Supplementary Tables S1-S3).

73 The basalts major element composition also varies with age, the older samples being  
74 poorer in sodium than the younger ones.  $Na_8$ , an inverse proxy of the degree of melting  
75 experienced by the mantle column<sup>7,8</sup> (Supplementary Table S2), is on average lower in the  
76 VLS older basalts; thus, they were apparently produced by a degree of melting higher than  
77 the younger basalts (Supplementary Fig. S1a). However,  $Na_8$  has been defined for a  
78 homogeneous lherzolitic source<sup>8</sup>. A heterogeneous source generates complex melt mixing  
79 patterns depending on the relative extent of melting, homogenisation and enrichment of  
80 each component<sup>16-18</sup>. For this reason we adopt here the expression “apparent” degree of  
81 melting.

82 The proxy equivalent (but reverse) to basalt  $Na_8$  is in peridotites the Cr#  
83 ( $Cr\# = Cr/(Cr+Al)$ ) of spinels and pyroxenes<sup>9,10</sup>. During the last 26 Ma, peridotite spinel  
84 Cr# increased along the VLS on average from 22 to 37 (Supplementary Fig S1c)  
85 suggesting that the amount of magma delivered at ridge axis increased through time, in  
86 agreement with gravity profiles running along spreading-flow-lines (Supplementary Fig.  
87 S1c), revealing that crustal thickness increased from  $4.8 \pm 0.2$  km in the 22-27 Ma interval  
88 to  $5.4 \pm 0.2$  km between 0-5 Ma<sup>1,4</sup>.

89 Based on calibrations of Warren, 2016<sup>19</sup>, the degree of melting ( $F_{max}$ ) of the VLS  
90 peridotites increased from 8.0 to 14.2 F% toward younger crustal ages (average 10.8, Fig.  
91 2). MORB glasses  $Na_8$  increased with time along the VLS from 2.6 to 3.0 on average  
92 (Supplementary Fig. S1a).  $F_{max}$  in the basalts can be estimated according to<sup>7</sup> and compared  
93 to the  $F_{max}$  of the mantle peridotites. Comparing temporal sections of mantle residua and of  
94 their melt products must take into account a time-delay in the emplacement of the mantle

95 peridotites in the oceanic crust. According to<sup>1,4</sup> we corrected the crustal ages of the mantle  
96 rocks relative to that of basalts by a relative time lag of 2.2 Ma (see online Methods: Age  
97 Correction).

98 The calculated apparent  $F_{\max}$  of MORB glasses vary little during the 26 Ma-long VLS  
99 stretch (Fig. 1b) with values ranging from 18.0 to 15.8 F% (ave. 16.7), significantly higher  
100 than those estimated from mantle residual peridotites (Fig. 1b). A striking feature of the  
101  $\text{Na}_8$  degree of melting curve is the decrease of the apparent  $F_{\max}$  through time that  
102 countertrends with both the associated mantle peridotites degree of melting curve and the  
103 gravity-inferred crustal thickness (Fig. 1b; Supplementary Fig. S1c).

104

#### 105 Significance of the decoupling

106

107 The degrees of melting estimated from the mantle peridotites and from the basalts can  
108 be generated by variations of mantle potential temperature, mantle composition and  
109 spreading rate. Changes in mantle temperature or source fertility will result in coherent  
110 changes of the degrees of melting estimated from basalts and from peridotites. Similarly,  
111 changes in spreading rate cannot decouple the behaviour of residual mantle and extracted  
112 basalts, because, in a passive upwelling scenario, decreasing the spreading rate lowers the  
113 thermal state of the entire melting region, and vice versa<sup>20</sup>. During the last 26 Ma the half  
114 spreading rate at the EMAR segment decreased from 17.2 mm/a (Chron 6) to 16.9 mm/a  
115 (Chron 5) to present-day 13.6 mm/a<sup>21,22</sup> (Supplementary Fig. S1b). Such decrease of  
116 spreading rate toward younger ages should lower the mantle degree of melting by about  
117 1%<sup>20</sup>; thus, the increase in degree of melting recorded by the VLS mantle peridotites must  
118 be caused by processes other than changes in spreading rate, mantle temperature or  
119 fertility.

120 We consider now a heterogeneous mantle source. Thermodynamic modelling of  
121 melting a two-component mantle source predicts that when a fertile heterogeneity, i.e.  
122 pyroxenite, starts melting, the temperature of the whole mantle parcel is lowered due to the  
123 latent heat of melting<sup>15</sup>. If the heterogeneity is less than a few kilometres, some heat is  
124 transferred from the peridotite into the melting heterogeneity increasing its melt  
125 productivity while cooling the surrounding mantle<sup>13-15</sup>. Accordingly, the vertical interval  
126 where only pyroxenites undergo melting represents an undercooling region whose extent is  
127 proportional to the amount of pyroxenites (Fig. 2). It follows that, for a given P-T  
128 decompression path, the degree of melting undergone by a homogeneous peridotitic

129 mantle is higher than the degree of melting of the same peridotite but veined by  
130 pyroxenites.

131 A lithologically homogeneous mantle source, resulting in coherent estimates of the  
132 degree of melting between peridotites and basalt proxies, is approximated in the younger  
133 (< 5 Ma) portion of the VLS where both basalt- and peridotite-derived F% converge  
134 toward a common value. We assume that the present-day subridge mantle (Vema  
135 Unveined Mantle or VUM) contains negligible amounts of pyroxenites, not sufficient to  
136 perturb thermally the melting process of the host mantle peridotite. Thus, for this region  
137 the Na<sub>8</sub>-derived degree of melting is in line with its original interpretation<sup>7,8,23</sup>.

138 In contrast, in a veined mantle scenario, degrees of melting estimated from peridotites  
139 and from basalts differ strongly. While the Cr# records the true F<sub>max</sub> of the ambient  
140 peridotite, the pooled melts aggregate the compositional signal of both (low F) peridotitic  
141 and (high F) pyroxenitic melts<sup>18</sup>. We propose that the low degree of melting of the older  
142 portion of the VLS peridotites is due to heat consumption during preferential melting of a  
143 pyroxenitic component at nearly constant mantle potential temperature. Along the VLS we  
144 have decreasing quantities of pyroxenites injected into the melting region, with consequent  
145 decrease of the undercooling effect and expansion of the anhydrous peridotite melting  
146 region.

147 We tested this hypothesis by modelling the decompressive adiabatic melting of a mixed  
148 source based on the experimental-parameterized algorithm Melt-PX<sup>24</sup>. Mantle potential  
149 temperatures have been constrained using the passive flow temperature field model of  
150 Bonatti et al., (2003)<sup>1</sup> giving a mantle T<sub>p</sub> = 1350 °C. For this temperature and a lherzolithic  
151 source containing 15% clinopyroxene, Melt-PX calculations overestimate crustal thickness  
152 and mantle degrees of melting observed at the EMAR segment (Fig. 3). These calculations  
153 assume that melting ceases at the base of the crust, a boundary condition acceptable for  
154 high mantle T<sub>p</sub> settings as in fast spreading ridges or hotspots<sup>24,25</sup>. They represent the  
155 model maximum allowed thickness at a given thermal setting (Fig. 3). Mantle flow  
156 models<sup>1,26</sup> predict the end of melting to occur at P<sub>f</sub> ≈ 0.7 GPa, well below the base of the  
157 crust. This condition applies to low-spreading ridges due to heat conduction to the surface  
158 resulting in a deep transition from the conductive to the convective thermal region<sup>20,26–28</sup>.

159 As low-melting component we adopted the silica deficient pyroxenite M7-16<sup>29</sup> for  
160 reasons defined in the next section. We observe that an increase in the fraction  $X_p$  of  
161 pyroxenite in the mantle is paralleled by a decrease of degree of melting of the host

162 peridotite ( $F_r$ ) (Fig. 3) depending also on the final pressure of melting (varying in the  
163 range 0.3-1.1 GPa, Fig. 3).

164 Integration of the melt productivity of the host peridotite and of the pyroxenite along an  
165 adiabatic path, weighted by their relative abundance, allows estimating magmatic crustal  
166 thickness. Lambart et al., (2016)<sup>24</sup> show that the total magmatic productivity increases  
167 proportionally to the amount of pyroxenite in the source. This observation apparently is in  
168 contrast with the increase toward younger ages along the VLS of gravity-inferred crustal  
169 thickness, paralleled by a decrease of the estimated amount of pyroxenites dispersed within  
170 the mantle (Fig. 2, Supplementary Fig. S1c). This contradiction is solved considering that  
171 increasing the amount of low-melting lithologies enhances the undercooling of the host  
172 peridotitic mantle due to heat diffusion into the melting pyroxenite<sup>13</sup>. Undercooling  
173 estimated by Melt-PX calculations can reach up to 40 °C for adiabatic melting under the  
174 assumed conditions. Reduced undercooling due to a decrease of the mantle pyroxenite  
175 fraction during melting results in shallowing the final pressure of melting from  $\approx 1.1$  to 0.7  
176 GPa going from the oldest to the youngest VLS sectors (Fig. 3, right panel).

177 These observations and numerical experiments reveal that in slow-spreading ridges, at  
178 constant mantle potential temperature, the arrival of a pulse of pyroxenites in the mantle  
179 source region will cause a reduction of crustal thickness. The countertrend of crustal  
180 thickness and degree of mantle melting with spreading rate along the VLS is a positive test  
181 of our hypothesis.

182

183

184 Composition of the low-solidus component and effects on Na8

185

186 The effect of pyroxenite-derived melts on the final composition of the pooled MORB  
187 depends upon the nature of the heterogeneities and on their dilution in the peridotite-  
188 derived melt<sup>17,30-32</sup>. In mid-ocean ridge settings most pyroxenites produce melts with  
189 major-element composition similar to those derived from peridotite<sup>33</sup>. Hence, little  
190 reactivity is expected when pyroxenite-derived melts mix with mantle peridotite-derived  
191 melts<sup>34</sup>. We thus explore the possible composition of pyroxenites dispersed in the VLS  
192 mantle by considering mixing of silica-deficient (SD) and silica-enriched (SE) pyroxenite-  
193 derived melts with peridotite-derived melts. In a Na<sub>2</sub>O versus MgO diagram, young VLS

194 lavas plot at higher Na<sub>2</sub>O content than the older ones (Supplementary Fig. S2). We assume  
195 that the youngest VLS Na-rich lavas, i.e. those showing a degree of melting similar to that  
196 of the associated peridotites, derive from melting of the VUM source defining a peridotite  
197 primitive melt composition that matches the VUM average Na<sub>8</sub> and F% (Supplementary  
198 Table S2). We then calculated mixing lines between the VUM primitive melt and  
199 pyroxenitic-derived melts obtained experimentally at variable degrees of melting from  
200 different sources (Supplementary Fig. S2-S3). Melt mixing affects the estimated Na<sub>8</sub>, and  
201 consequently the estimated apparent degree of melting, depending on the absolute Na  
202 content and Mg/Na ratio of the added melt fraction (Supplementary Fig. S3). Inferred Na<sub>8</sub>  
203 and apparent F of the mixed compositions show that SE-derived melts do not reproduce  
204 the observed variability for reasonable fractions and degrees of melting of the pyroxenitic-  
205 derived components (Supplementary Fig. S3). Among the SD pyroxenites only those  
206 having high Mg/Na ratios, as M7-16, match the VLS observed variability. It is worth  
207 noting that the mixed melts matching the VLS data are those obtained at high F (F=65%),  
208 a value close to those predicted by thermodynamics<sup>13-15</sup>. Based on these calculation the  
209 VLS variability can be approximated by linear mixing of a VUM primitive melt with ca.  
210 30% M7-16 type pyroxenite-derived melt.

211

212

### 213 Size and nature of mantle domains

214

215 An important result of thermodynamic modelling<sup>13,14</sup> is that the undercooling inferred  
216 from F% decoupling occurs only for a composite source where a lower-T solidus  
217 component is finely dispersed in a high-T-solidus host to ensure efficient heat diffusion.  
218 Adopting the calibration of<sup>13</sup> for tabular heterogeneities limits their size to be < 1 km, a  
219 dimension close to those estimated from seismic scatter (<10 km)<sup>35</sup>. Cryptic stripes of  
220 comparable size (4 km) have been described at the SEIR<sup>36</sup> and modelled based on Nd-Hf  
221 MORB variability by<sup>37</sup>. The compositional trend observed along the VLS suggests a  
222 decreasing decoupling of the measured parameters. The lateral extension of the melting  
223 region reaches 300 km in the spreading direction, ca. 70 km along axis<sup>26</sup>. A single large  
224 heterogeneity in the older mantle section would have measured tens of km in width,  
225 excluding efficient heat diffusion within the heterogeneity itself. We deduce that the older  
226 mantle section contained a cluster of small, tabular, low-T solidus components as in Figure  
227 2, decreasing in time from ca. 15% to 0% of the volume.

228 VLS basalts  $^{143}\text{Nd}/^{144}\text{Nd}$  versus  $^{208}\text{Pb}/^{206}\text{Pb}$  ratios duplicate one of the mixing trends  
229 recognized in South Atlantic basalt suites<sup>38,39</sup> (Supplementary Fig. S4), suggesting that  
230 those endmembers are ubiquitous in the sub-Atlantic mantle.

231 VLS glasses  $^{143}\text{Nd}/^{144}\text{Nd}$  and  $^{87}\text{Sr}/^{86}\text{Sr}$  ratios vary in a restricted range (0.51295-  
232 0.51317 and 0.70258-0.70351 respectively, Fig. 1, S5, Online Methods); in contrast,  
233 mantle peridotite clinopyroxenes display a large scatter ( $^{143}\text{Nd}/^{144}\text{Nd}$ : 0.512024-0.513616;  
234  $^{87}\text{Sr}/^{86}\text{Sr}$ : 0.702220-0.705508, age corrected values). This different compositional scatter  
235 can be generated by chromatographic dispersion in the melting column<sup>40</sup> or through time  
236 by reactive melt infiltration and veining<sup>41,42</sup>.

237 The VLS oldest basalts show the highest apparent degree of melting and the most  
238 enriched Sr-Nd-Pb isotopic signature (Supplementary Fig. S4-S5). We suggest that their  
239 compositions reflect a larger contribution of pyroxenite-derived melts. As a result, the  
240 peridotites of the older domain are less affected by decompression melting, and record  
241 lower degrees of melting, possibly preserving their original DMM isotopic fingerprint. In  
242 contrast, the VLS younger basalts received a negligible contribution of pyroxenite-derived  
243 melts. Unfortunately, we do not have enough data on the mantle peridotites of this young  
244 VLS stretch because they are still buried below the sea floor; however the few available  
245 samples indicate that this parcel of peridotitic mantle underwent high degree of melting.

246

247

248

249 Distribution of pyroxenites along Mid Ocean Ridges

250

251 We attempt now to extend our findings to other portions of the mid ocean ridge system  
252 and interpret the chemistry of genetically related basalt/peridotite in terms of the  
253 proportion of pyroxenite dispersed in the mantle source. Only two stretches of the global  
254 MOR system have basalt-peridotite pairs sampled densely enough to allow first order  
255 observations: the northern Mid Atlantic and the Southwest Indian Ridges<sup>19,43</sup>. In both cases  
256 along axis mantle peridotites record an extent of melting systematically lower than that  
257 recorded by the associated basalts (Fig. 4).

258 In light of our findings we propose that pyroxenites are widely distributed in subridge  
259 mantle sources proportionally to  $\Delta F_{\pi}^{\beta} = F_{\beta}^{app} - F_{\pi}$  the difference between the degree of  
260 melting derived from basalts and that derived from peridotites (see Online Methods). This

261 interpretation, if correct, should be confirmed by a correlation between the extent of  $\Delta F_{\pi}^{\beta}$   
262 and chemical indicators of the presence of pyroxenite in the source, e.g. the isotopic ratios  
263 of radiogenic elements, expected to be enriched in recycled materials. A broad negative  
264 correlation appears between the measured  $\Delta F_{\pi}^{\beta}$  and the basalt  $^{143}\text{Nd}/^{144}\text{Nd}$  ratios (Fig. 5,  
265 Supplementary Table S4 ), suggesting the dependence of the Nd isotopic composition on  
266  $\Delta F_{\pi}^{\beta}$  ( $r^2=0.53$ ) and revealing similar enriching mechanisms in the two ridge systems.

267 Spreading rate and mantle potential temperature may not be the leading factors  
268 affecting the composition of the extracted basalts and of the residual mantle: the relative  
269 proportion of pyroxenites versus peridotites in the mantle source maybe more important. A  
270 major implication is that at constant temperature a pulse of low-melting pyroxenite  
271 entering the melting region may not lead to a pulse of magmatism because the increased  
272 undercooling of the mantle shrinks the peridotitic melting region contrasting the increase  
273 of instantaneous pyroxenite melt production.

274 Our results show that low-T melting heterogeneities dispersed in the mantle source  
275 affect not only the composition of the extracted basaltic melts, but also the total extent of  
276 melting, the volume of extracted melts, and consequently crustal thickness.

277

278

#### 279 Acknowledgments

280 This work has been supported by Italian-PRIN prot. 2015C5LN35 and by the U.S.  
281 National Science Foundation under grant no. OCE-05-51288. We are also grateful for the  
282 support of the Deep Energy community of the Carbon Observatory funded by Alfred P.  
283 Sloan Foundation. We thank Charlie Langmuir, Henry Dick, Jessica Warren and Monique  
284 Seyler, for stimulating insightful discussions and critical reading of an early version of the  
285 work. We are grateful to Marco Ligi for his support on geophysics and Sarah Lambart for  
286 helping on Melt-PX. We also thank S. Lambart, A. Stracke and an anonymous reviewer  
287 for their constructive reviews that greatly improved the manuscript. We are grateful to A.  
288 Whitchurch for the editorial assistance. This is Lamont-Doherty contribution number xxx.

289

#### 290 Author contributions

291 D.B. performed the modelling. A.C. analysed the samples. D.B. and A.C. processed the  
292 geochemical data and wrote jointly the paper. E.B. provided the opportunity and support  
293 for sea-expeditions and work. All the authors discussed the results and the interpretations.

294

295

296

## 298 References

299

- 300 1. Bonatti, E. *et al.* Mantle thermal pulses below the Mid-Atlantic Ridge and temporal variations in the  
301 formation of oceanic lithosphere. *Nature* **423**, 499–505 (2003).
- 302 2. Brunelli, D., Seyler, M., Cipriani, A., Ottolini, L. & Bonatti, E. Discontinuous Melt Extraction and  
303 Weak Refertilization of Mantle Peridotites at the Vema Lithospheric Section (Mid-Atlantic Ridge).  
304 *J. Petrol.* **47**, 745–771 (2006).
- 305 3. Bonatti, E. *et al.* Flexural uplift of a lithospheric slab near the Vema transform (Central Atlantic):  
306 Timing and mechanisms. *Earth Planet. Sci. Lett.* **240**, 642–655 (2005).
- 307 4. Cipriani, A., Bonatti, E., Brunelli, D. & Ligi, M. 26 million years of mantle upwelling below a  
308 segment of the Mid Atlantic Ridge: The Vema Lithospheric Section revisited. *Earth Planet. Sci. Lett.*  
309 **285**, 87–95 (2009).
- 310 5. Cipriani, A., Brueckner, H. K., Bonatti, E. & Brunelli, D. Oceanic crust generated by elusive parents:  
311 Sr and Nd isotopes in basalt-peridotite pairs from the Mid-Atlantic Ridge. *Geology* **32**, 657–660  
312 (2004).
- 313 6. Cipriani, A. *et al.* A 19 to 17 Ma amagmatic extension event at the Mid-Atlantic Ridge: Ultramafic  
314 mylonites from the Vema Lithospheric Section. *Geochemistry Geophys. Geosystems* **10**, (2009).
- 315 7. Plank, T. & Langmuir, C. H. Effects of the melting regime on the composition of the oceanic crust. *J.*  
316 *Geophys. Res.* **97**, 19749–19770 (1992).
- 317 8. Klein, E. M. & Langmuir, C. H. Global correlations of ocean ridge basalt chemistry with axial depth  
318 and crustal thickness. *J. Geophys. Res.* **92**, 8089 (1987).
- 319 9. Dick, H. J. B. & Bullen, T. Chromian spinel as a petrogenetic indicator in abyssal and alpine-type  
320 peridotites and spatially associated lavas. *Contrib. to Mineral. Petrol.* **86**, 54–76 (1984).
- 321 10. Michael, P. J. & Bonatti, E. Peridotite composition from the North Atlantic: regional and tectonic  
322 variations and implications for partial melting. *Earth Planet. Sci. Lett.* **73**, 91–104 (1985).
- 323 11. Katz, R. F. & Weatherley, S. M. Consequences of mantle heterogeneity for melt extraction at mid-  
324 ocean ridges. *Earth Planet. Sci. Lett.* **335–336**, 226–237 (2012).
- 325 12. Weatherley, S. M. & Katz, R. F. Melting and channelized magmatic flow in chemically  
326 heterogeneous, upwelling mantle. *Geochemistry Geophys. Geosystems* **13**, Q0AC18 (2012).
- 327 13. Katz, R. F. & Rudge, J. F. The energetics of melting fertile heterogeneities within the depleted  
328 mantle. *Geochemistry Geophys. Geosystems* **12**, 1–22 (2011).
- 329 14. Phipps Morgan, J. Thermodynamics of pressure release melting of a veined plum pudding mantle.  
330 *Geochemistry Geophys. Geosystems* **2**, (2001).
- 331 15. Sleep, N. H. Tapping of Magmas from Ubiquitous Mantle Heterogeneities : An alternative to Mantle  
332 plumes? *J. Geophys. Res.* **89**, 10029–10041 (1984).
- 333 16. Ito, G. & Mahoney, J. J. Flow and melting of a heterogeneous mantle: 1. Method and importance to  
334 the geochemistry of ocean island and mid-ocean ridge basalts. *Earth Planet. Sci. Lett.* **230**, 29–46  
335 (2005).

- 336 17. Shorttle, O. Geochemical variability in MORB controlled by concurrent mixing and crystallisation.  
337 *Earth Planet. Sci. Lett.* **424**, 1–14 (2015).
- 338 18. Rudge, J. F., MacLennan, J. & Stracke, A. The geochemical consequences of mixing melts from a  
339 heterogeneous mantle. *Geochim. Cosmochim. Acta* **114**, 112–143 (2013).
- 340 19. Warren, J. M. Global Variations in Abyssal Peridotite Compositions. *Lithos* **248–251**, 193–219  
341 (2016).
- 342 20. Bown, J. W. & White, R. S. Variation with spreading rate of oceanic crustal thickness and  
343 geochemistry. *Earth Planet. Sci. Lett.* **121**, 435–449 (1994).
- 344 21. Cande, S. C., LaBrecque, J. L. & Haxby, W. F. Plate kinematics of the South Atlantic: Chron C34 To  
345 Present. *J. Geophys. Res. Solid Earth* **93**, 13479–13492 (1988).
- 346 22. Cande, S. C. & Kent, D. V. Revised calibration of the geomagnetic polarity timescale for the Late  
347 Cretaceous and Cenozoic. *J. Geophys. Res. Solid Earth* **100**, 6093–6095 (1995).
- 348 23. Langmuir, C. H., Klein, E. M. & Plank, T. in *Mantle Flow and Melt Generation at Mid-Ocean*  
349 *Ridges* (ed. Morgan, J. P.) 183–280 (American Geophysical Union, 1992).
- 350 24. Lambart, S., Baker, M. B. & Stolper, E. M. The role of pyroxenite in basalt genesis: Melt-PX, a  
351 melting parameterization for mantle pyroxenites between 0.9 and 5 GPa. *J. Geophys. Res. Solid*  
352 *Earth* **121**, 0–28 (2016).
- 353 25. Shorttle, O. & MacLennan, J. Compositional trends of Icelandic basalts: Implications for short-length  
354 scale lithological heterogeneity in mantle plumes. *Geochemistry, Geophys. Geosystems* **12**, (2011).
- 355 26. Ligi, M., Cuffaro, M., Chierici, F. & Calafato, A. Three-dimensional passive mantle flow beneath  
356 mid-ocean ridges: an analytical approach. *Geophys. J. Int.* **175**, 783–805 (2008).
- 357 27. McKenzie, D. & Bickle, M. J. The volume and composition of melt generated by extension of the  
358 lithosphere. *J. Petrol.* **29**, 625–679 (1988).
- 359 28. Shen, Y. & Forsyth, D. W. Geochemical constraints on initial and final depths of melting beneath  
360 mid-ocean ridges. *J. Geophys. Res.* **100**, 2211–2237 (1995).
- 361 29. Lambart, S., Laporte, D. & Schiano, P. Markers of the pyroxenite contribution in the major-element  
362 compositions of oceanic basalts: Review of the experimental constraints. *Lithos* **160–161**, 14–36  
363 (2013).
- 364 30. Stracke, A., Bourdon, B. & McKenzie, D. Melt extraction in the Earth's mantle: Constraints from U-  
365 Th-Pa-Ra studies in oceanic basalts. *Earth Planet. Sci. Lett.* **244**, 97–112 (2006).
- 366 31. Stracke, A. & Bourdon, B. The importance of melt extraction for tracing mantle heterogeneity.  
367 *Geochim. Cosmochim. Acta* **73**, 218–238 (2009).
- 368 32. Rubin, K. H., Sinton, J. M., MacLennan, J. & Hellebrand, E. Magmatic filtering of mantle  
369 compositions at mid-ocean-ridge volcanoes. *Nat. Geosci.* **2**, 321–328 (2009).
- 370 33. Lambart, S., Laporte, D. & Schiano, P. An experimental study of pyroxenite partial melts at 1 and  
371 1.5GPa: Implications for the major-element composition of Mid-Ocean Ridge Basalts. *Earth Planet.*  
372 *Sci. Lett.* **288**, 335–347 (2009).
- 373 34. Lambart, S., Laporte, D., Provost, a. & Schiano, P. Fate of Pyroxenite-derived Melts in the  
374 Peridotitic Mantle: Thermodynamic and Experimental Constraints. *J. Petrol.* **53**, 451–476 (2012).
- 375 35. Helffrich, G. R. & Wood, B. J. The Earth's mantle. *Nature* **412**, 501–7 (2001).

- 376 36. Graham, D. W., Blichert-Toft, J., Russo, C. J., Rubin, K. H. & Albarede, F. Cryptic striations in the  
377 upper mantle revealed by hafnium isotopes in southeast Indian ridge basalts. *Nature* **440**, 199–202  
378 (2006).
- 379 37. Liu, B. & Liang, Y. The prevalence of kilometer-scale heterogeneity in the source region of MORB  
380 upper mantle. 1–8 (2017).
- 381 38. Hoernle, K. *et al.* On- and off-axis chemical heterogeneities along the South Atlantic Mid-Ocean-  
382 Ridge (5–11°S): Shallow or deep recycling of ocean crust and/or intraplate volcanism? *Earth Planet.*  
383 *Sci. Lett.* **306**, 86–97 (2011).
- 384 39. Paulick, H., Münker, C. & Schuth, S. The influence of small-scale mantle heterogeneities on Mid-  
385 Ocean Ridge volcanism: Evidence from the southern Mid-Atlantic Ridge (7°30'S to 11°30'S) and  
386 Ascension Island. *Earth Planet. Sci. Lett.* **296**, 299–310 (2010).
- 387 40. Liang, Y. Simple models for dynamic melting in an upwelling heterogeneous mantle column:  
388 Analytical solutions. *Geochim. Cosmochim. Acta* **72**, 3804–3821 (2008).
- 389 41. Borghini, G. *et al.* Meter-scale Nd isotopic heterogeneity in pyroxenite-bearing Ligurian peridotites  
390 encompasses global-scale upper mantle variability. *Geology* **41**, 1055–1058 (2013).
- 391 42. Borghini, G. *et al.* Pyroxenite Layers in the Northern Apennines' Upper Mantle (Italy)—Generation  
392 by Pyroxenite Melting and Melt Infiltration. *J. Petrol.* **57**, 625–653 (2016).
- 393 43. Gale, A., Langmuir, C. H. & Dalton, C. A. The global systematics of ocean ridge basalts and their  
394 origin. *J. Petrol.* **55**, 1051–1082 (2014).
- 395
- 396

398 **Figure captions**

399

400 **Figure 1:** Figure 1. a) Temporal variation of the VLS basaltic glasses  $^{143}\text{Nd}/^{144}\text{Nd}$   
 401 isotopic ratios. Solid circles define three domains (average Nd isotopic ratio of each sector  
 402 is indicated). Dashed line is average of oldest sector without one enriched sample.

403 b) Temporal variation of the degree of melting as inferred by mantle peridotite  
 404 residues<sup>19</sup> and erupted MORBs<sup>7</sup>. Each point represents a dredge average. Thick bold lines  
 405 are linear regressions; thin lines show 95% confidence bands. The age of mantle rocks is  
 406 corrected for the time lag between their arrival at the seafloor and the arrival of the basaltic  
 407 melts they produced according to <sup>1,4</sup> (see Methods).

408

409

410 **Figure 2:** Interpretative sketch of the upwelling mantle column below the Vema  
 411 Lithospheric Section. At constant mantle potential temperature the presence of pyroxenites  
 412 causes a contraction of the melting region. Total degree of decompressive adiabatic  
 413 melting is computed based on Melt-PX algorithm<sup>24</sup>. In the older VLS sectors, the onset of  
 414 melting of the mantle peridotite is delayed and its degree of melting reduced ( $F_{\text{max}}=8$ ). The  
 415 associated pyroxenite melts more ( $F_{\text{max}}=53$ ) and contributes to the higher apparent degree  
 416 of melting in the pooled MORBs. Undercooling of the mantle peridotite causes deepening  
 417 of the end of the melting column estimated to shallow by 0.4 GPa from the older to the  
 418 younger sector.

419

420

421 **Figure 3:** Melt-PX<sup>24</sup> numerical experiments for adiabatic melting of a two-component  
 422 mantle source: lherzolite plus SD pyroxenite (M7-16<sup>29</sup>). The thick black line represents the  
 423 model limit value for melting ceasing at the base of the crust.

424 Left Panel: the degree of melting of the host peridotite is lowered by adding up to 40%  
 425 pyroxenite in the source. Variable extents of the melting column are computed assuming  $P_f$   
 426 from 1.1 to 0.3 GPa. Red dashed lines correspond to the VLS average melting interval  
 427 from old ( $F_{\text{max}}=8.0$ ) to young ( $F_{\text{max}}=14.2$ ) sectors.

428 Panel B: Variation of the aggregated crustal thickness as function of pyroxenite fraction  
429 in the source and final depth of melting. Average values for the VLS extremes are plotted  
430 as red symbols and  $1\sigma$  standard deviation

431

432 **Figure 4:** Variation of the degree of melting estimated from mantle peridotite (blue  
433 dots) and associated basalts (red dots) along the Southwest Indian Ridge (upper) and the  
434 Mid Atlantic Ridge from the Equator to the Azores hotspot region (lower). Degrees of  
435 melting are calculated based on <sup>19,23,43</sup> on data compiled from PetDB  
436 ([www.earthchem.org/petdb](http://www.earthchem.org/petdb)). Variations of the amount of low-T melting heterogeneities  
437 (pyroxenite) in the source result in larger differences in the estimated degree of melting  
438 ( $\Delta F_r^\beta$ ), a proxy for the along axis pyroxenite vol% content of the source.

439

440 **Figure 5:** Difference of degree of melting estimated from genetically related basalts and  
441 peridotites ( $\Delta F$ ) versus the Nd isotopic composition of basalt. The VLS sectors are plotted  
442 as large red circles; delta F increases from sector 1 to 3 (young to old). Black diamonds  
443 represent SWIR, blue circles MAR. Regression lines are calculated for the whole  
444 population (red solid line), the SWIR (black solid line) and the MAR (blue solid line).  
445 Data and parameters in supplementary Table S4; 95% confidence bands are plotted in  
446 Supplementary Fig. S6. Our interpretation is that the  $\Delta F$  between basalt and peridotite is a  
447 proxy of the amount of low-T solidus pyroxenites in the source.

448

449

## 450 **METHODS**

451

### 452 **Analytical Methods**

453 Major elements

454 Major elements on mineral phases were collected with the electron probe (Cameca SX100)  
455 at the American Museum of Natural History (NY) using 15kV acceleration voltage, 20nA  
456 beam, a 10 $\mu$ m diameter beam and 30 s counting times. Sodium, potassium and chlorine  
457 were run under different conditions to attain a higher precision and monitor their mobility,  
458 with a 5nA beam and counting times of 80 s. A subset of samples has been analysed with a  
459 Cameca X-Five microprobe at the CAMPARIS micro-analytical center (University of  
460 Paris VI), following procedures detailed in <sup>44</sup>. A number of primary mineral standards  
461 were used, as well as the MORB JDF-D2 standard.

462 Isotope ratios

463 For isotopic determinations 50 to 250 mg of basaltic glass and clinopyroxene separate  
464 were prepared by grinding, sieving and handpicking under a binocular microscope. Glass  
465 chips were leached in 8N HNO<sub>3</sub>. Clinopyroxenes were treated with three leachates to  
466 eliminate the effects of seawater alteration <sup>5,45</sup>. Pb was separated using AG1-X8 anion  
467 resin, Sr was separated using Eichrom Sr resin and Nd was separated in a two-column  
468 procedure using Eichrom TRU-spec resin to separate the rare-earth elements, followed by  
469  $\alpha$ -hydroxy isobutyric acid. Isotopes were measured on a VG Sector 54 multicollector mass  
470 spectrometer housed at the Lamont Doherty Earth Observatory of Columbia University. Sr  
471 and Nd isotopes were measured in multidynamic mode. The mass fractionation corrections  
472 were based on <sup>86</sup>Sr/<sup>88</sup>Sr = 0.1194 and <sup>146</sup>Nd/<sup>144</sup>Nd = 0.7219. Over the period of analytical  
473 work, repeated analyses yielded a <sup>87</sup>Sr/<sup>86</sup>Sr ratio of 0.710271  $\pm$  0.000015 for the NBS-987  
474 Sr standard (2 $\sigma$  external reproducibility, n>22) and a <sup>143</sup>Nd/<sup>144</sup>Nd ratio of 0.512096  $\pm$   
475 0.000023 for the JNdi-1 (2 $\sigma$  external reproducibility, n>38). Total blanks for Sr and Nd did  
476 not exceed 80pg. Pb data on basaltic glasses were collected in static mode, using the  
477 double spike technique with the calibrated 207/204 spike. Replicate analyses of the Pb  
478 isotope standard NBS981 gave an average of 16.9317 $\pm$ 0.0022 and 15.4912 $\pm$ 0.0027 and  
479 36.7060 $\pm$ 0.0066 for <sup>206</sup>Pb/<sup>204</sup>Pb, <sup>207</sup>Pb/<sup>204</sup>Pb, and <sup>208</sup>Pb/<sup>204</sup>Pb, respectively. These measured  
480 Pb isotope ratios were corrected to the values defined by <sup>46</sup> of 16.9356, 15.4891, and  
481 36.7006, respectively, for NBS 981. Reproducibility for NBS981 is 130, 174, and 181 ppm  
482 (2 $\sigma$ , N=47), for <sup>206</sup>Pb/<sup>204</sup>Pb, <sup>207</sup>Pb/<sup>204</sup>Pb, and <sup>208</sup>Pb/<sup>204</sup>Pb ratios, respectively. Pb blanks  
483 measured were below 100pg and thus negligible relative to the amount of sample analysed.

484

### 485 **Estimate of the $\Delta F_{\pi}^{\beta}$ and <sup>143</sup>Nd/<sup>144</sup>Nd of the associated basalts**

486 Figure 4 of the main text reports the correlation between  $\Delta F_{\pi}^{\beta}$ , as the differential in degree  
487 of melting between basalt and peridotites, and the Nd isotopic composition of basalts of  
488 several portions of the Mid Ocean Ridge system where both basalts and peridotites have

489 been sampled. Among all the explored ridge segments, only few localities report basalts  
490 and mantle peridotites sampled in the same dredge haul or site. Basaltic rocks are generally  
491 more abundant and present a much denser lateral sampling than mantle peridotites. Basalt  
492 chemistry and isotopic ratios appear to vary systematically over variable length scale  
493 defining domains in which they show little variability or monotonic changes along the  
494 ridge axis (e.g. <sup>43, 47-48</sup> among others). Domains characterized by reduced variability of the  
495 chemical character of the basalts are usually bounded by major transform faults, which  
496 also act as thermal barriers<sup>47,49-51</sup>. Therefore, in Figure 4 (main text), we have chosen to  
497 integrate the dataset of the sites where peridotites and basalts were sampled together with  
498 sites where only mantle rocks were recovered, but for which is possible to infer the  
499 isotopic composition of the associated basalts from the regional variability. As a  
500 conservative approach, we only considered those domains in which lateral isotopic and  
501 compositional variability is very low or described by simple monotonic trends.  
502 The degree of melting of mantle-peridotites can be affected by Cr# fluctuations due to  
503 melt/rock interaction that modify spinel<sup>9</sup> and pyroxene compositions<sup>52</sup>. Therefore we  
504 filtered spinel composition and applied a threshold of TiO<sub>2</sub><0.15 wt% as discussed in <sup>2,19</sup>.  
505 The supplementary Table S4, reports the inferred values showing the measured and  
506 calculated value for each basalt-peridotite couple. The “regional regression” data are  
507 calculated considering sets of neighboring peridotites and basalts, whereas the “local  
508 average” set of data refers to basalts and peridotites sampled from the same site. ±σ on  
509  $\Delta F_{\pi}^{\beta}$  are estimated by error propagation.

510

### 511 **Age correction**

512 Basalts from the VLS were erupted over a time range of 26 Ma. We applied, hence, an age  
513 correction for radiogenic ingrowth since the closure of the system to allow comparisons of  
514 their initial isotopic composition, which is controlled only by the source. The correction  
515 time should be calculated since the closure of the system, represented by the moment of  
516 separation between the source and the melt at depth, assuming there was no significant  
517 melt-rock interaction thereafter. This is attested by mantle residual rocks from the VLS  
518 being all equilibrated in the spinel field showing no late interaction with melts. The only  
519 report of plagioclase-equilibrated mantle rocks concerns the strain-driven formation of  
520 plagioclase in fertile lherzolites during mylonitization<sup>53</sup>. We identify the melt-source  
521 separation at the estimated upper limit of melting as inferred by modelling with Melt-PX  
522 (see main text).

523 Based on the estimation of melting a composite source and varying the position of the end  
524 of the melting column between 1.2 and 0.3 GPa, it appears that the end of the melting  
525 column can be constrained based on the correlation with the measured crustal thickness  
526 and degree of melting of the residual mantle. For the time stretch relative to the VLS the  
527 end of the melting column can be set at 1.1 GPa for the older domain and 0.7 GPa for the  
528 younger domain. Based on Africa-South America Euler vectors of <sup>21</sup> and the geomagnetic  
529 time scale of <sup>22</sup>, the spreading rate at the EMAR axis can be estimated through time. As  
530 shown in Figure 1 of the main text, the spreading rate decreased steadily in the last 30 Ma.  
531 The absolute value decreases from 17.2 to 16.9 mm/y at Chron 6 (half spreading rate) and

532 from 16.9 to 13.6 mm/y at Chron 5. Crustal ages can be calculated accordingly during this  
533 time stretch assuming basalts erupted in the axial region.

534 Times of extraction for the mantle residue and for the basalts are, however, very different.  
535 Ascent rates for the basaltic liquids are estimated in the range of m/y<sup>54-56</sup>. Setting the  
536 melt/source separation at 1.1 and 0.7 GPa and upwelling rates in the range 1-5 m/y<sup>56</sup> gives  
537 upwelling times ranging 7-36 ka for the older VLS domain and 5-23 ka for the younger  
538 VLS domain. Such delays are unimportant in the age correction of long-time decay  
539 systems as those here discussed (Sm-Nd; Rb-Sr; U-Pb); however, we considered this  
540 contribution for the total age correction when discussing age corrected values in Figs 1B  
541 and S1.

542 Upwelling of the mantle lasts a significant amount of time and can sensibly modify the  
543 isotopic relationships. The time necessary for a mantle parcel to join the crust from the end  
544 of melting depth is 2.1 Ma for the older VLS domain and 1.7 Ma for the younger VLS  
545 domain.

546

547

548

549

## 551 References

552

- 553 44. Seyler, M. & Brunelli, D. Sodium–chromium covariation in residual clinopyroxenes from abyssal  
554 peridotites sampled in the 43°–46°E region of the Southwest Indian Ridge. *Lithos* **302–303**, 142–157  
555 (2018).
- 556 45. Cipriani, A., Bonatti, E. & Carlson, R. W. Nonchondritic <sup>142</sup>Nd in suboceanic mantle peridotites.  
557 *Geochemistry, Geophys. Geosystems* **12**, 1–8 (2011).
- 558 46. Todt, W., Cliff, R., Hanser, A. & Hofmann, A. W. Evaluation of a 202Pb–205Pb double spike for  
559 high - precision lead isotope analysis. *Geophys. Monogr. Ser.* **95**, 429–437 (1996).
- 560 47. Meyzen, C. M. *et al.* New insights into the origin and distribution of the DUPAL isotope anomaly in  
561 the Indian Ocean mantle from MORB of the Southwest Indian Ridge. *Geochem. Geophys. Geosyst.*  
562 **6**, Q11K11 (2005).
- 563 48. Meyzen, C. M., Toplis, M. J., Humler, E., Ludden, J. N. & Mevel, C. A discontinuity in mantle  
564 composition beneath the southwest Indian ridge. *Nature* **421**, 731–733 (2003).
- 565 49. Cannat, M., Rommevaux-Jestin, C., Sauter, D., Deplus, C. & Mendel, V. Formation of the axial  
566 relief at the very slow spreading Southwest Indian Ridge (49° to 69°E). *J. Geophys. Res.* **104**,  
567 22825–22843 (1999).
- 568 50. Seyler, M., Brunelli, D., Toplis, M. J. & Mével, C. Multiscale chemical heterogeneities beneath the  
569 eastern Southwest Indian Ridge (52°E–68°E): Trace element compositions of along-axis dredged  
570 peridotites. *Geochemistry, Geophys. Geosystems* **12**, (2012).
- 571 51. Paquet, M., Cannat, M., Brunelli, D., Hamelin, C. & Humler, E. Effect of melt/mantle interactions on  
572 MORB chemistry at the easternmost Southwest Indian Ridge (61°–67°E). *Geochemistry, Geophys.*  
573 *Geosystems* **17**, (2016).
- 574 52. Brunelli, D., Paganelli, E. & Seyler, M. Percolation of enriched melts during incremental open-  
575 system melting in the spinel field: A REE approach to abyssal peridotites from the Southwest Indian  
576 Ridge. *Geochim. Cosmochim. Acta* **127**, 190–203 (2014).
- 577 53. Cannat, M. & Seyler, M. Transform tectonics, metamorphic plagioclase and amphibolitization in  
578 ultramafic rocks of the Vema transform fault (Atlantic Ocean ). *Earth Planet. Sci. Lett.* **133**, 283–298  
579 (1995).
- 580 54. Spiegelman, M. & Kenyon, P. The requirements for chemical disequilibrium during magma  
581 migration. *Earth Planet. Sci. Lett.* **109**, 611–620 (1992).
- 582 55. Spiegelman, M. & Elliott, T. Consequences of melt transport for uranium series disequilibrium in  
583 young lavas. *Earth Planet. Sci. Lett.* **118**, 1–20 (1993).
- 584 56. Lundstrom, C. C., Gill, J., Williams, Q. & Perfit, M. R. Mantle Melting and Basalt Extraction by  
585 Equilibrium Porous Flow. *Science (80-. )*. **270**, 1958 LP-1961 (1995).

586

587

588

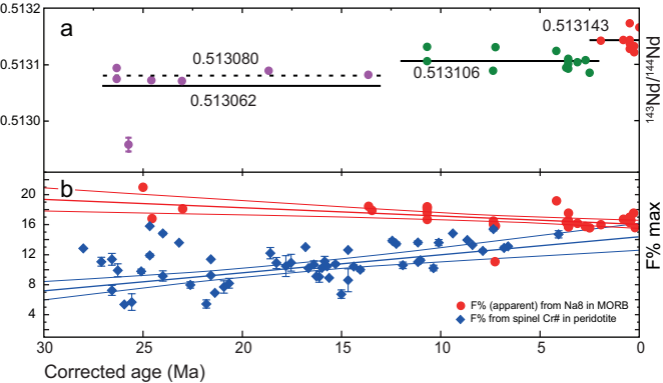


Fig. 1

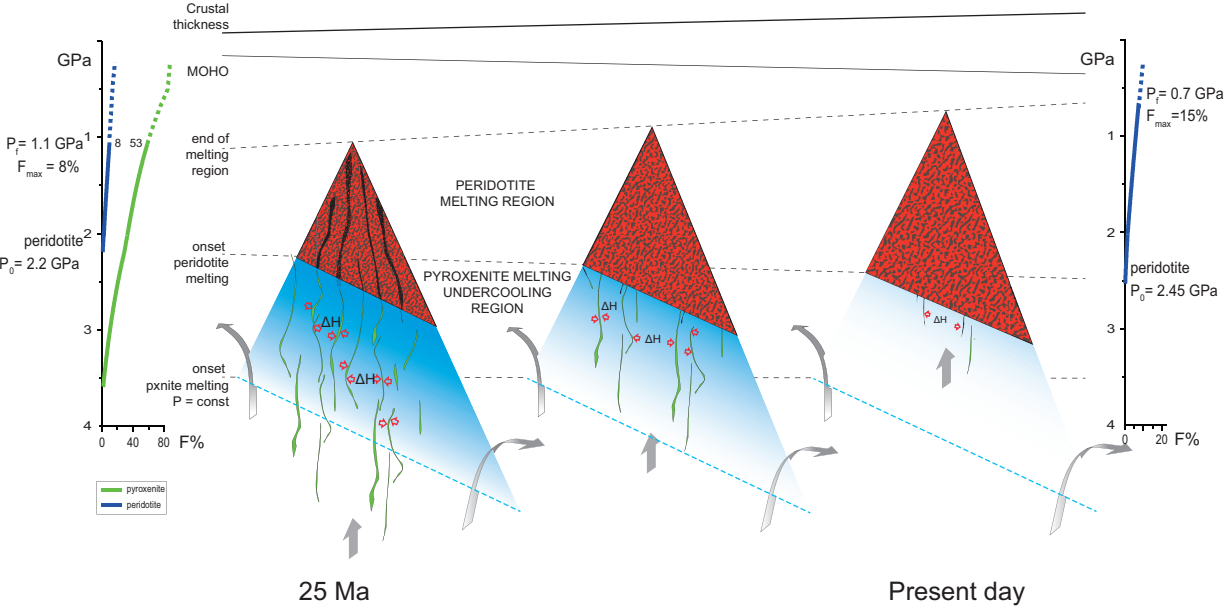


Figure 2 - last

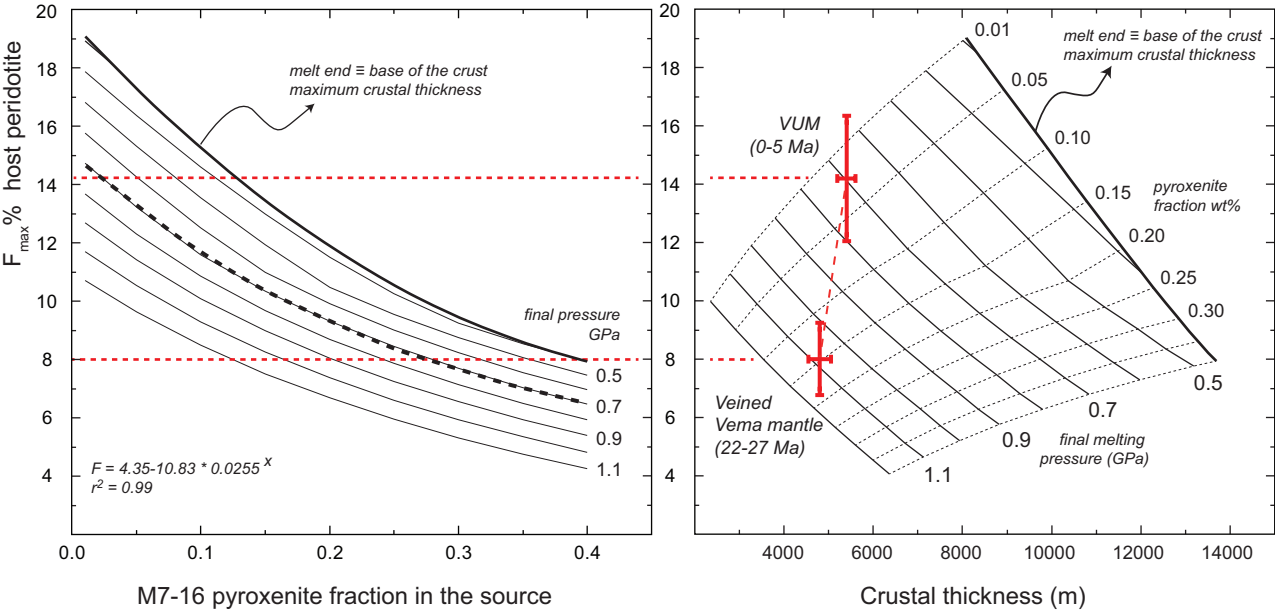


Figure 3\_last

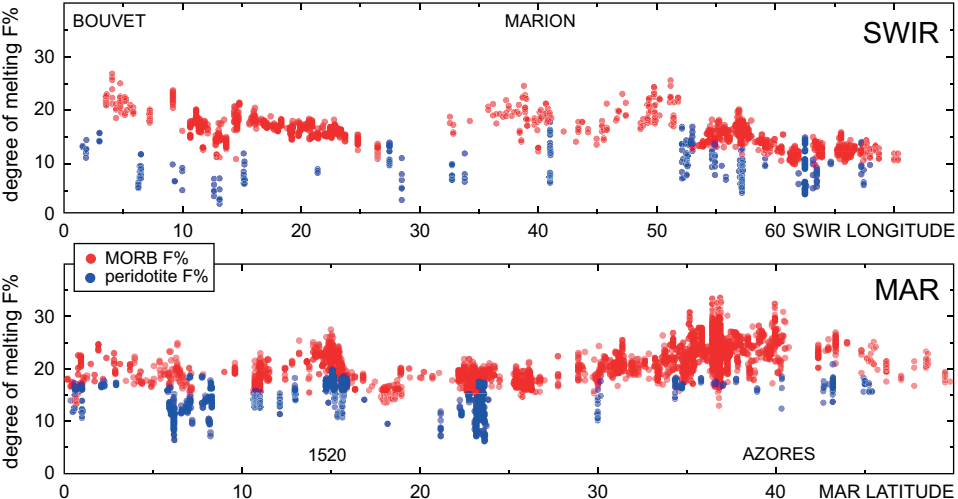


Figure 4-last

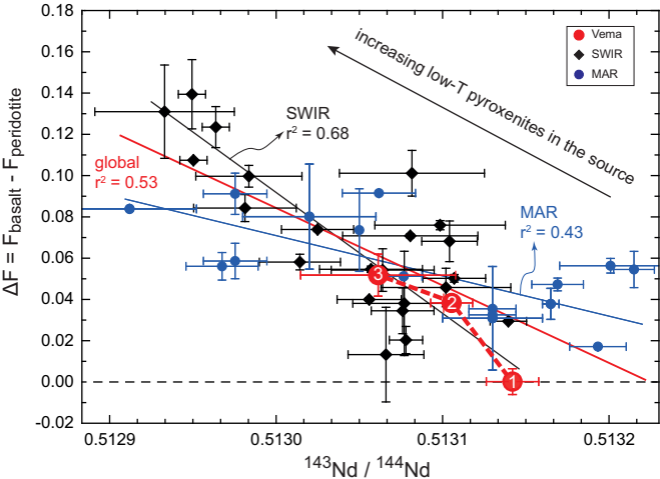


Figure 5 - last